Supporting Information for

Hyperbolic-enhanced Raman scattering in van der Waals $MoOCl_2$: from Fano resonances to picomolar detection

Anton Minnekhanov[1†], Gleb Tikhonowski[1†], Georgy Ermolaev[1†], Konstantin V. Kravtsov[1], Gleb Tselikov[1], Adilet Toksumakov[1], Aleksandr Slavich[1], Ivan Kazantsev[1], Andrey Vyshnevyy[1], Ivan Kruglov[1], Ilya Radko[1], Zdenek Sofer[2], Aleksey Arsenin[1], Kostya S. Novoselov[3,4,5], Valentyn Volkov[1*]*

[1]*Emerging Technologies Research Center, XPANCEO, Internet City, Emmay Tower, Dubai, United Arab Emirates*

[2]*Department of Inorganic Chemistry, University of Chemistry and Technology Prague, Technická 5, 166 28 Prague 6, Czech Republic*

[3]*National Graphene Institute (NGI), University of Manchester, Manchester, M13 9PL, U.K.*

[4]*Department of Materials Science and Engineering, National University of Singapore, Singapore, 03-09 EA, Singapore*

[5]*Institute for Functional Intelligent Materials, National University of Singapore, 117544, Singapore, Singapore*

[†]These authors contributed equally to this work

[*]*Correspondence should be addressed to e-mail: kostya@nus.edu.sg and vsv@xpanceo.com*

Contents

Supplementary Notes

Supplementary Note SN1. First-principles calculations and Raman tensor formalism for $MoOCl_2$.

From the computed phonon band structure (**Figure SN1**) and analysis of the irreducible representations of the Γ-point modes, we selected the Raman-active modes. For the intensity calculations, primitive (not unit) cell with atoms displaced along each Raman-active vibration was used. Its lattice parameters are as follows: a=b=6.63181 Å, c=6.524 Å, α=β=104.18°, γ=32.89°. These cells are shown in **Figure SN2**.

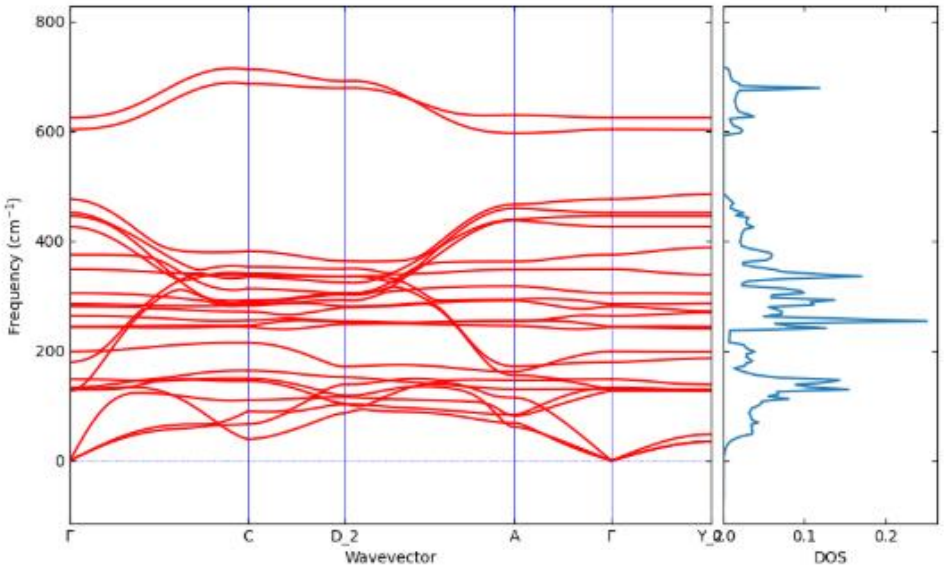

Figure SN1. Phonon band structure and density of states of bulk $MoOCl_2$.

For $MoOCl_2$ with the C2/m (B2/m, see below) space group, the irreducible representation of Γ-point phonons is the following:

$$\Gamma = \Gamma_{acoustic} + \Gamma_{optic},$$

$$\Gamma_{acoustic} = A_u + 2B_u,$$

$$\Gamma_{optic} = 3A_u + 6B_u + 8A_g + 4B_g.$$

Only the A_g and B_g modes are Raman-active, and we calculated their intensities. Computed peak positions are shown in **Table SN1** together with their intensities. Only five modes in the experiment have sufficient intensity in the spectral range from 100 to 500 cm^{-1}. Evaluated intensities based on Placzek's approximation (as implemented in Phonopy-Spectroscopy) for frequency-dependent dielectric tensor show good agreement with experimental Raman spectrum (see **Figure 1d** and **Table SN1**). We note here that there is a mode of sufficient intensity in DFT at around 305 cm^{-1}. In the experiment we observe a peak of around 301 cm^{-1}. However, in the experiment its intensity is low and it is mixed with the overtone peak originating from the silicon substrate.

Table SN1. Positions of experimental peaks (ν_{Exp}) and computed Raman-active peaks (ν_{DFT}) together with their irreducible representations (Ir.rep.) and intensities (I_{DFT}).

ν_{Exp}, cm^{-1}	ν_{DFT}, cm^{-1}	Ir. rep.	I_{DFT}, arb. units		
			532 nm	633 nm	785 nm
123	127	B_g	0.01	0.03	0.01
	131	B_g	0.00	0.00	0.00
	133	A_g	0.01	0.02	0.01
	148	B_g	0.00	0.00	0.00
177	199	A^1_g	1.00	1.00	1.00
	243	A_g	0.00	0.00	0.00
292	281	A^2_g	0.36	0.31	0.31
	305	A_g	0.06	0.05	0.02
351	349	A^3_g	0.74	0.45	0.21
431	445	A^4_g	0.19	0.22	0.25
	452	A_g	0.01	0.02	0.02
	624	B_g	0.00	0.02	0.05

In the reference work [1], the authors used a=12.721 Å, b=3.755 Å, c=6.524 Å, and β=104.86°. Thus, in their notation, the space group is C2/m. The axes order chosen in this work for the $MoOCl_2$ unit cell is a=3.755 Å, b=6.524 Å, c=12.721 Å, and α=104.86°. This is done for reasons of convenience so that the in-plane axes are a and b. From a crystallographic point of view, it corresponds to the B2/m space group. In such notation, a is a unique monoclinic axis. Therefore, for A_g and B_g modes of monoclinic lattices with a being the unique axis, Raman tensors are determined by the following expressions:

$$\hat{R}(A_g) = \begin{pmatrix} \tilde{a} & 0 & 0 \\ 0 & \tilde{b} & \tilde{d} \\ 0 & \tilde{d} & \tilde{c} \end{pmatrix}, \hat{R}(B_g) = \begin{pmatrix} 0 & \tilde{e} & \tilde{f} \\ \tilde{e} & 0 & 0 \\ \tilde{f} & 0 & 0 \end{pmatrix},$$

with $\tilde{a} = ae^{i\varphi_a}$, and a and φ_a are the absolute value and phase of $\tilde{a}$ respectively. This holds for all the rest of the components with tilde. Raman intensities in parallel configuration (VV) with $\hat{e}_i || \hat{e}_s = (\cos\theta \quad \sin\theta \quad 0)$ are as follows:

$$I^{||}(A_g) \sim \left|\tilde{a}\cos^2\theta + \tilde{b}\sin^2\theta\right|^2 = |a\cos^2\theta + b\cos\varphi_{ba}\sin^2\theta|^2 + b^2\sin^2\varphi_{ba}\sin^4\theta$$
$$I^{||}(B_g) \sim |\tilde{e}|^2\sin^2 2\theta$$

with $\varphi_{ba} = \varphi_b - \varphi_a$. For VH configuration $\hat{e}_i = (\cos\theta \quad \sin\theta \quad 0), \hat{e}_s = (-\sin\theta \quad \cos\theta \quad 0)$ intensities become:

$$I^{\perp}(A_g) \sim \left|\frac{\tilde{a}-\tilde{b}}{2}\sin 2\theta\right|^2 = \frac{a^2 - 2ab\cos\varphi_{ba} + b^2}{4}\sin^2 2\theta$$

$$I^{\perp}(B_g) \sim |\tilde{e}|^2 \cos^2 2\theta$$

These formulae describe equal lobe "✤" shapes. However, this is not observed in the experiment. It follows from the fact that the *c* axis is rotated relative to the out-of-plane (strictly orthogonal to the in-plane) direction by an angle of $\eta = \alpha - 90° = 14.86°$ around *a*-axis (see **Figure SN2**). Therefore, the Raman tensors should be rotated using the following rotation matrix:

$$\hat{S}(\eta) = \begin{pmatrix} 1 & 0 & 0 \\ 0 & \cos\eta & \sin\eta \\ 0 & -\sin\eta & \cos\eta \end{pmatrix}$$

using $\hat{S}^T(\eta)\hat{R}\,\hat{S}(\eta)$.

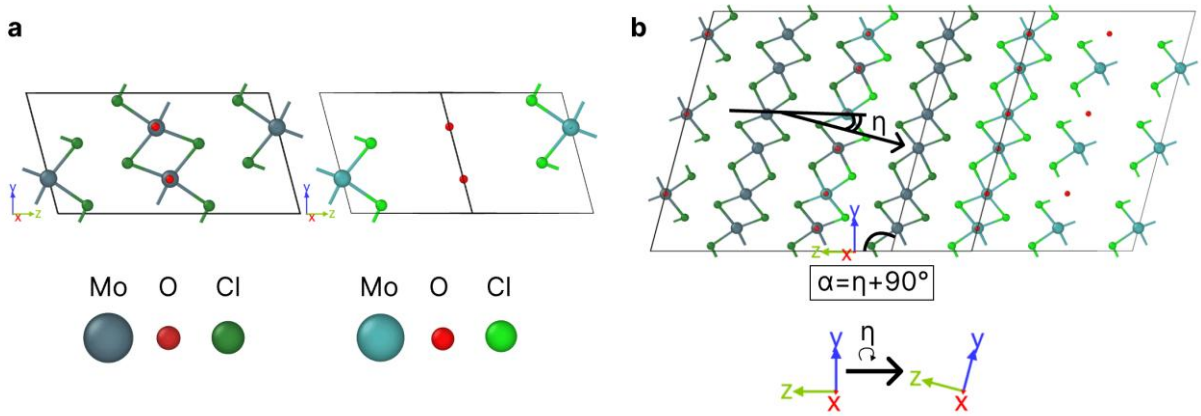

Figure SN2. a, Unit (left) and primitive (right) cells with distinct atom colorings. **b**, Supercells constructed from the unit and primitive cells, using the same color scheme as in **a**. The monoclinic angle α is expressed as $\eta + 90°$ ($\eta = 14.86°$). The black arrow denotes the light-propagation vector, orthogonal to the in-plane axis and forming an angle η with the z-axis. At the bottom, the rotation of the coordinate tripod by the angle η is shown.

After some algebra, it follows that the rotated Raman tensor for A_g modes keeps the same form, but with modified yy, yz and zz components. For the fitting, we need only the expressions for the rotated xx and yy components, which are:

$$\tilde{a}(\eta) = \tilde{a},$$
$$\tilde{b}(\eta) = F(\eta, \tilde{b}, \tilde{c}, \tilde{d}) = \cos\eta\,(\tilde{b}\cos\eta - \tilde{d}\sin\eta) - \sin\eta\,(\tilde{d}\cos\eta - \tilde{c}\sin\eta).$$

So, the intensity becomes:

$$I^{||}(A_g) \sim I_1(\eta)^2 + I_2(\eta)^2,$$

with

$$I_1(\eta) = a\cos^2\theta + \sin^2\theta\, F(\eta, b\cos\varphi_{ba}, c\cos\varphi_{ca}, d\cos\varphi_{da}) = a\cos^2\theta + F_{cos}\sin^2\theta,$$

$$I_2(\eta) = \sin^2\theta\, F(\eta, b\sin\varphi_{ba}, c\sin\varphi_{ca}, d\sin\varphi_{da}) = F_{sin}\sin^2\theta.$$

It is straightforward to represent F_{cos} and F_{sin} as: $F_{cos} = B\cos\varphi_{ba}$, $F_{sin} = C\sin\varphi_{ba}$. From now on, it immediately follows that the form of the VV intensity for the A_g modes is expressed as

$$I^{||}(A_g) \sim (A\cos^2\theta + B\cos\varphi_{ba}\sin^2\theta)^2 + C^2\sin^2\varphi_{ba}\sin^4\theta$$

This form is consistent with the Eq (2) from the main text.

The rotated Raman tensor for the B_g mode has all non-zero components except xx:

$$\hat{R}(B_g)(\eta) = \begin{pmatrix} 0 & \tilde{e}\cos\eta - \tilde{f}\sin\eta & \tilde{f}\cos\eta + \tilde{e}\sin\eta \\ \tilde{e}\cos\eta - \tilde{f}\sin\eta & 0 & 0 \\ \tilde{f}\cos\eta + \tilde{e}\sin\eta & 0 & 0 \end{pmatrix}$$

Thus, using this tensor, the intensities can be obtained easily. Here we provide the VV intensity expression for demonstration:

$$I^{||}(B_g) \sim \left|\tilde{e}\cos\eta - \tilde{f}\sin\eta\right|^2 \sin^2 2\theta,$$

bearing in mind that η is a fixed rotation angle.

References

1. Wang, Z. *et al.* Fermi liquid behavior and colossal magnetoresistance in layered MoOC l 2. *Phys. Rev. Mater.* **4**, 041001 (2020).

Supplementary figures

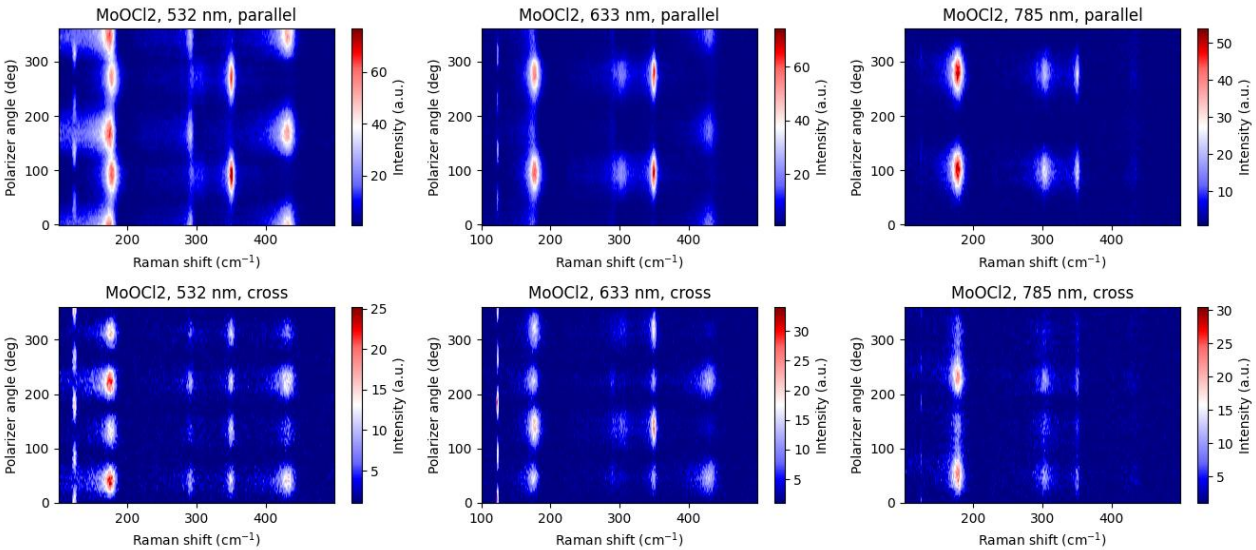

Figure S1. False-color maps of the parallel (VV) and cross (VH) Raman intensity at 532, 633, and 785 nm as a function of polarization angle and Raman shift in the $MoOCl_2$ exfoliated flake. The electric field is aligned with the *a* axis at polarization angles of 0° and 180°, and with the *b* axis at 90° and 270°.

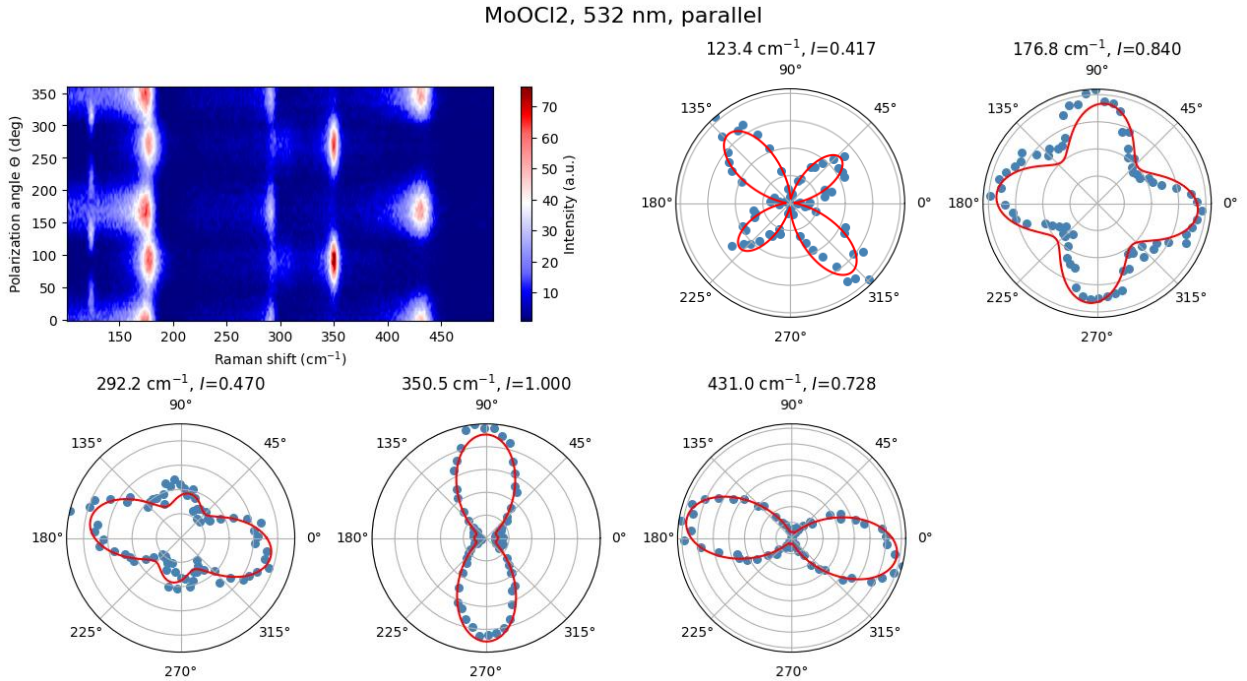

Figure S2. False-color map of the parallel (VV) Raman intensity at 532 nm (top left), and radar ARPR plots for all the Raman peaks of $MoOCl_2$ in this regime. The electric field is aligned with the *a* axis at polarization angles of 0° and 180°, and with the *b* axis at 90° and 270°.

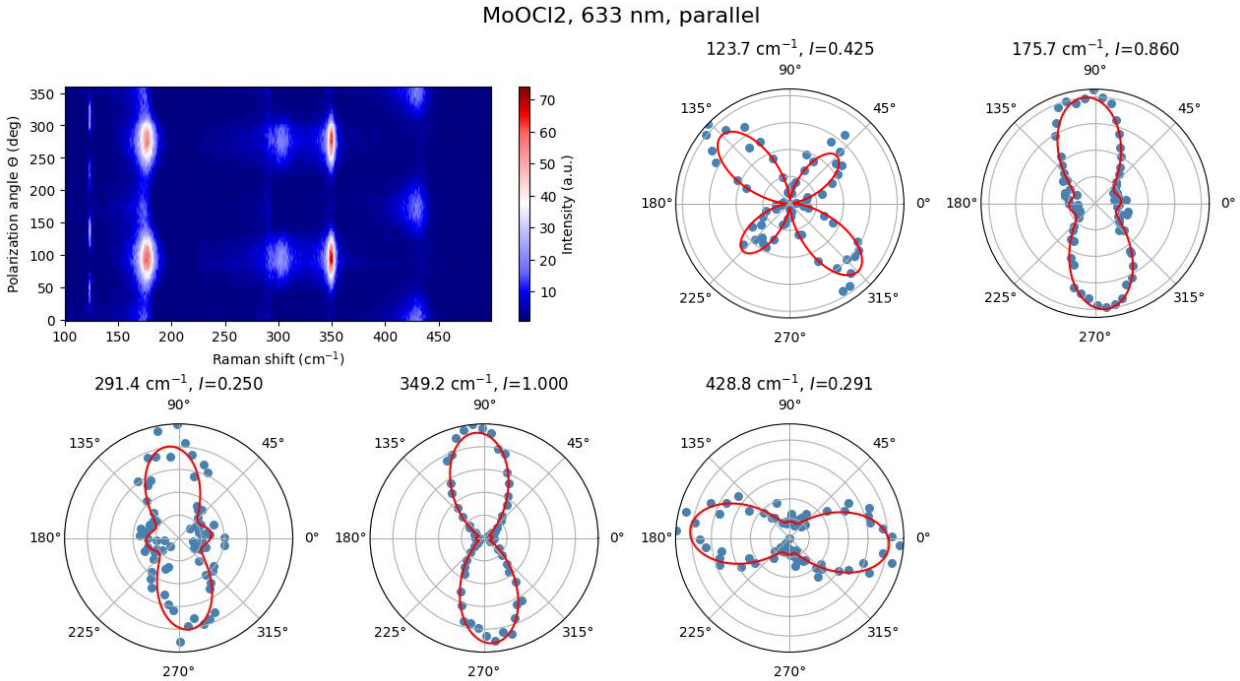

137 **Figure S3.** False-color map of the parallel (VV) Raman intensity at 633 nm (top left), and radar
138 ARPR plots for all the Raman peaks of $MoOCl_2$ in this regime. The electric field is aligned with
139 the *a* axis at polarization angles of 0° and 180°, and with the *b* axis at 90° and 270°.

140

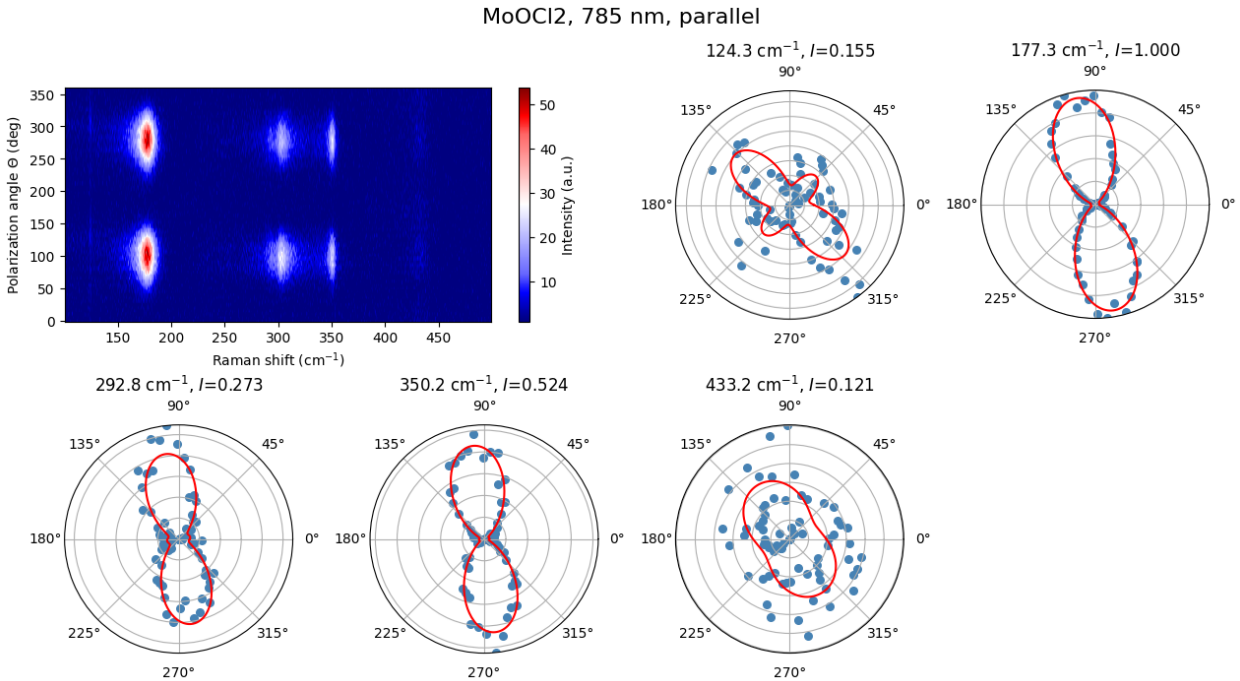

141 **Figure S4.** False-color map of the parallel (VV) Raman intensity at 785 nm (top left), and radar
142 ARPR plots for all the Raman peaks of $MoOCl_2$ in this regime. The electric field is aligned with
143 the *a* axis at polarization angles of 0° and 180°, and with the *b* axis at 90° and 270°.

144

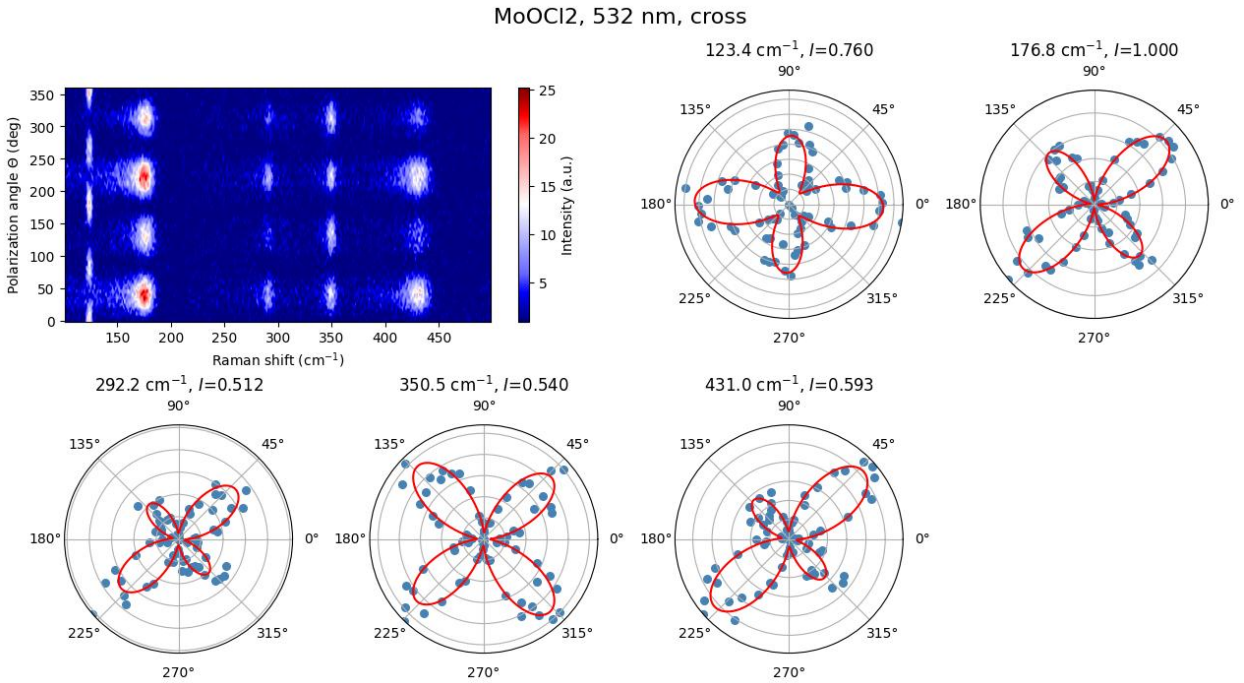

145 **Figure S5.** False-color map of the cross (VH) Raman intensity at 532 nm (top left), and radar
146 ARPR plots for all the Raman peaks of $MoOCl_2$ in this regime. The electric field is aligned with
147 the *a* axis at polarization angles of 0° and 180°, and with the *b* axis at 90° and 270°.

148

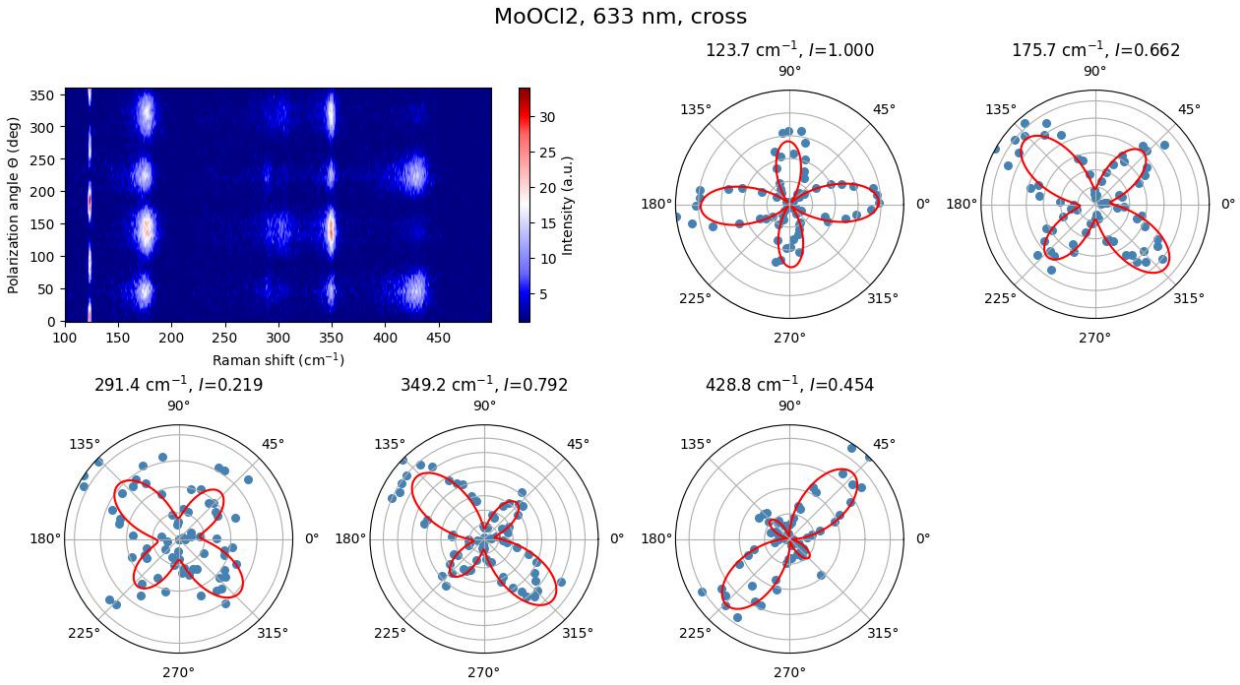

149

150 **Figure S6.** False-color map of the cross (VH) Raman intensity at 633 nm (top left), and radar
151 ARPR plots for all the Raman peaks of $MoOCl_2$ in this regime. The electric field is aligned with
152 the *a* axis at polarization angles of 0° and 180°, and with the *b* axis at 90° and 270°.

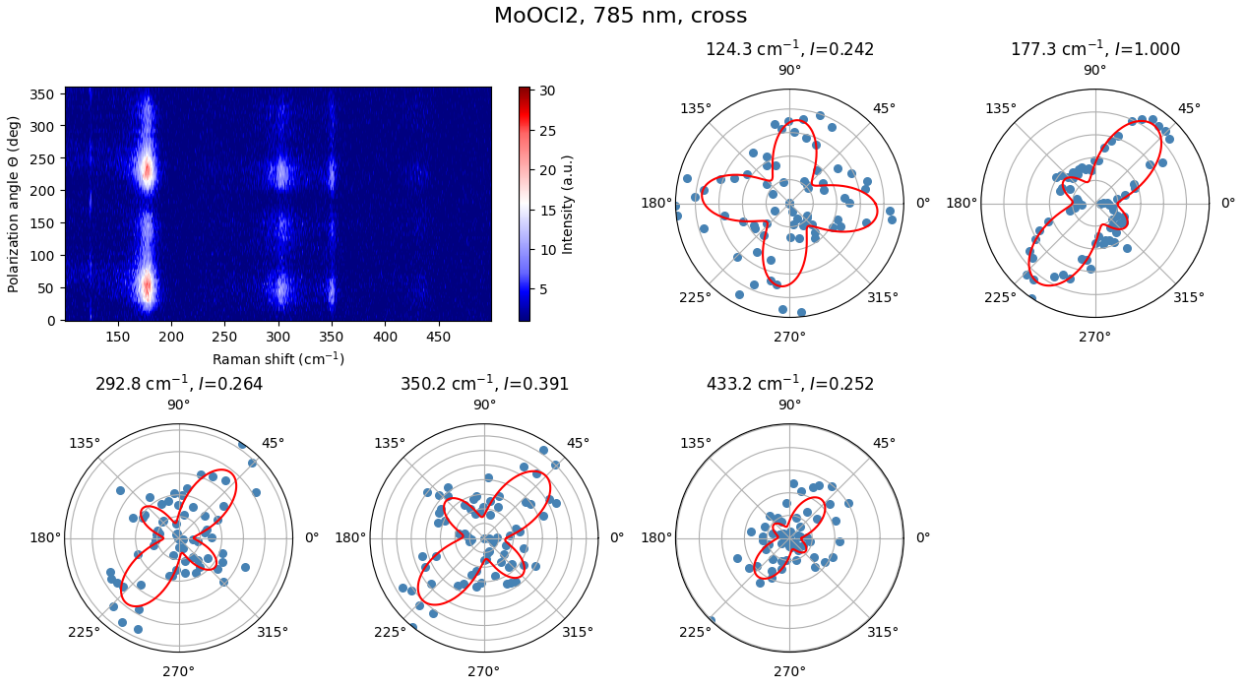

153

154 **Figure S7.** False-color map of the cross (VH) Raman intensity at 785 nm (top left), and radar
155 ARPR plots for all the Raman peaks of $MoOCl_2$ in this regime. The electric field is aligned with
156 the *a* axis at polarization angles of 0° and 180°, and with the *b* axis at 90° and 270°.

157

158

159

160

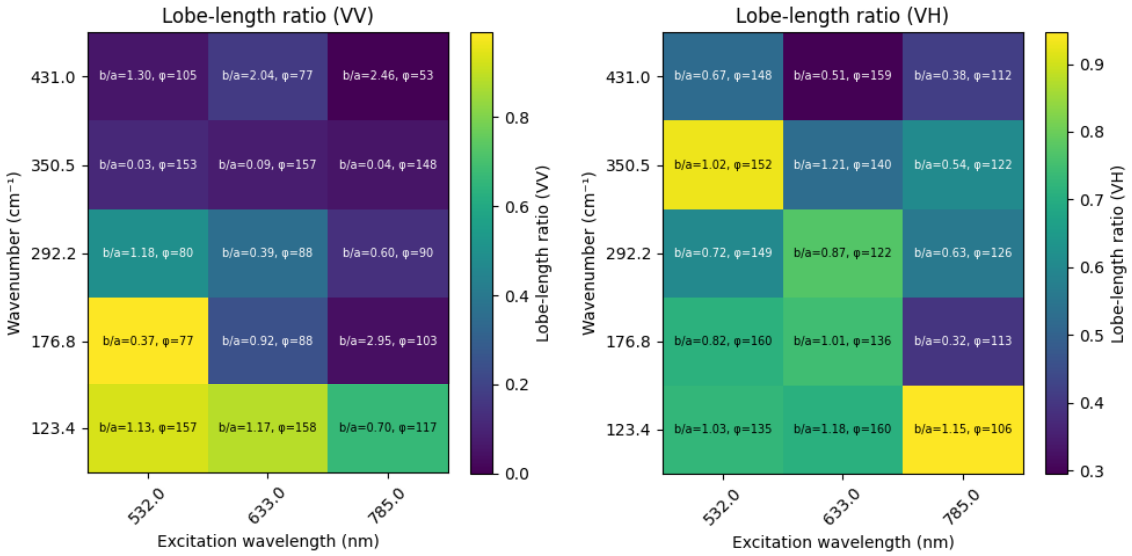

161 **Figure S8.** Heat maps of the lobe ratio parameter (0 and 1 correspond to 2-lobe and 4-lobe shapes,
162 respectively) for all Raman modes in $MoOCl_2$ as a function of excitation wavelength (columns)
163 and phonon frequency (rows) in the VV (left) and VH (right) regimes. Numbers inside the cells
164 list the fitting parameters b/a and φ_{ab} (Eq. (2)).

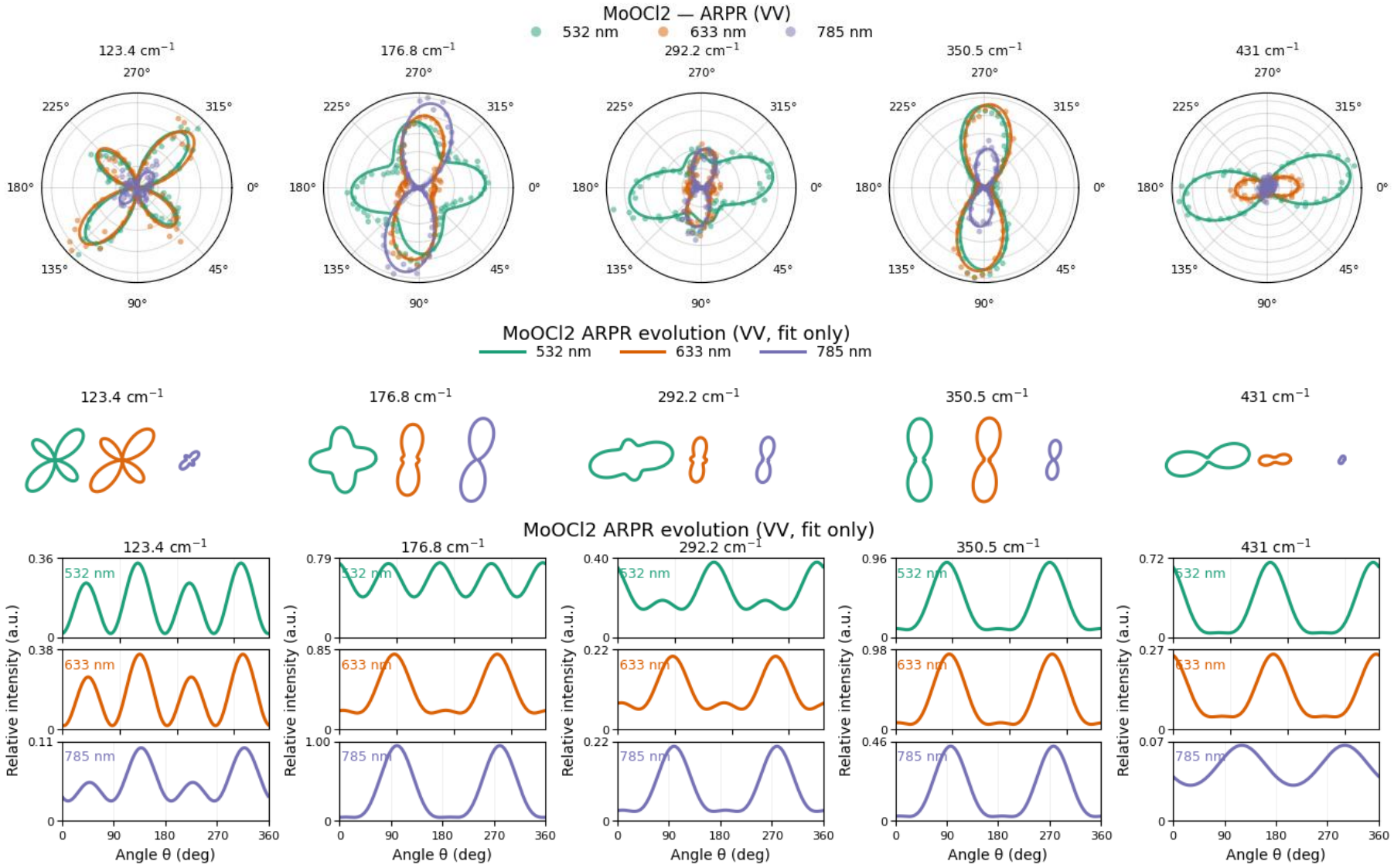

166 **Figure S9.** Top row: polar plots of the Raman modes of $MoOCl_2$ intensities at 532, 633, and 785 nm in the VV regime. Dots represent experimental
167 data, and solid curves – fit using Eq. (2). Middle row: schematic summary of this Raman-polarization switching (fits only). Bottom row: corresponding
168 one-dimensional angular cuts of the intensity for the three excitation wavelengths (fits only). The electric field is aligned with the *a* axis at polarization
169 angles of 0° and 180°, and with the *b* axis at 90° and 270°.

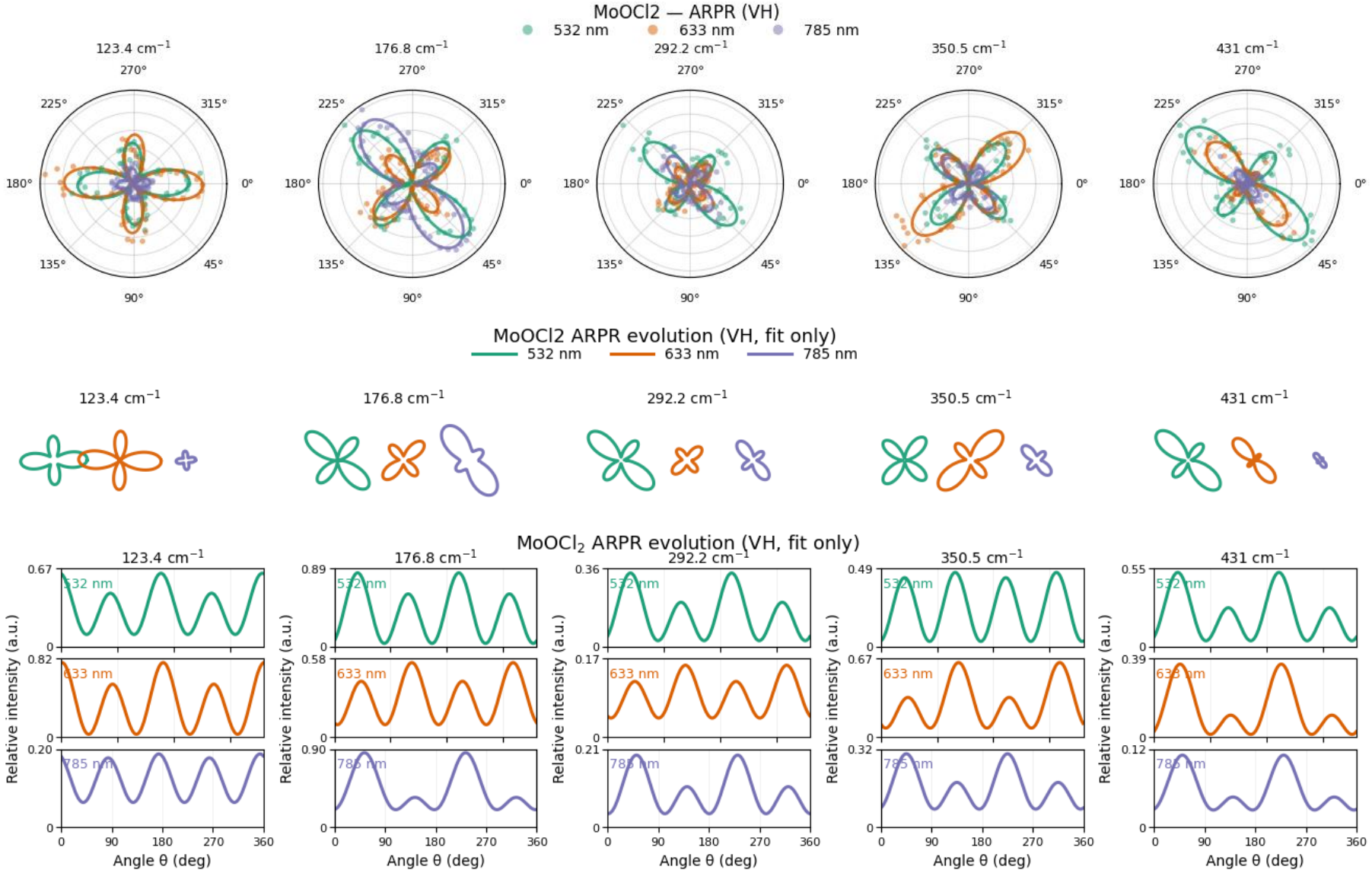

Figure S10. Top row: polar plots of the Raman modes of $MoOCl_2$ intensities at 532, 633, and 785 nm in the VH regime. Dots represent experimental data, and solid curves – fit using Eq. (2). Middle row: schematic summary of this Raman-polarization switching (fits only). Bottom row: corresponding one-dimensional angular cuts of the intensity for the three excitation wavelengths (fits only). The electric field is aligned with the *a* axis at polarization angles of 0° and 180°, and with the *b* axis at 90° and 270°.

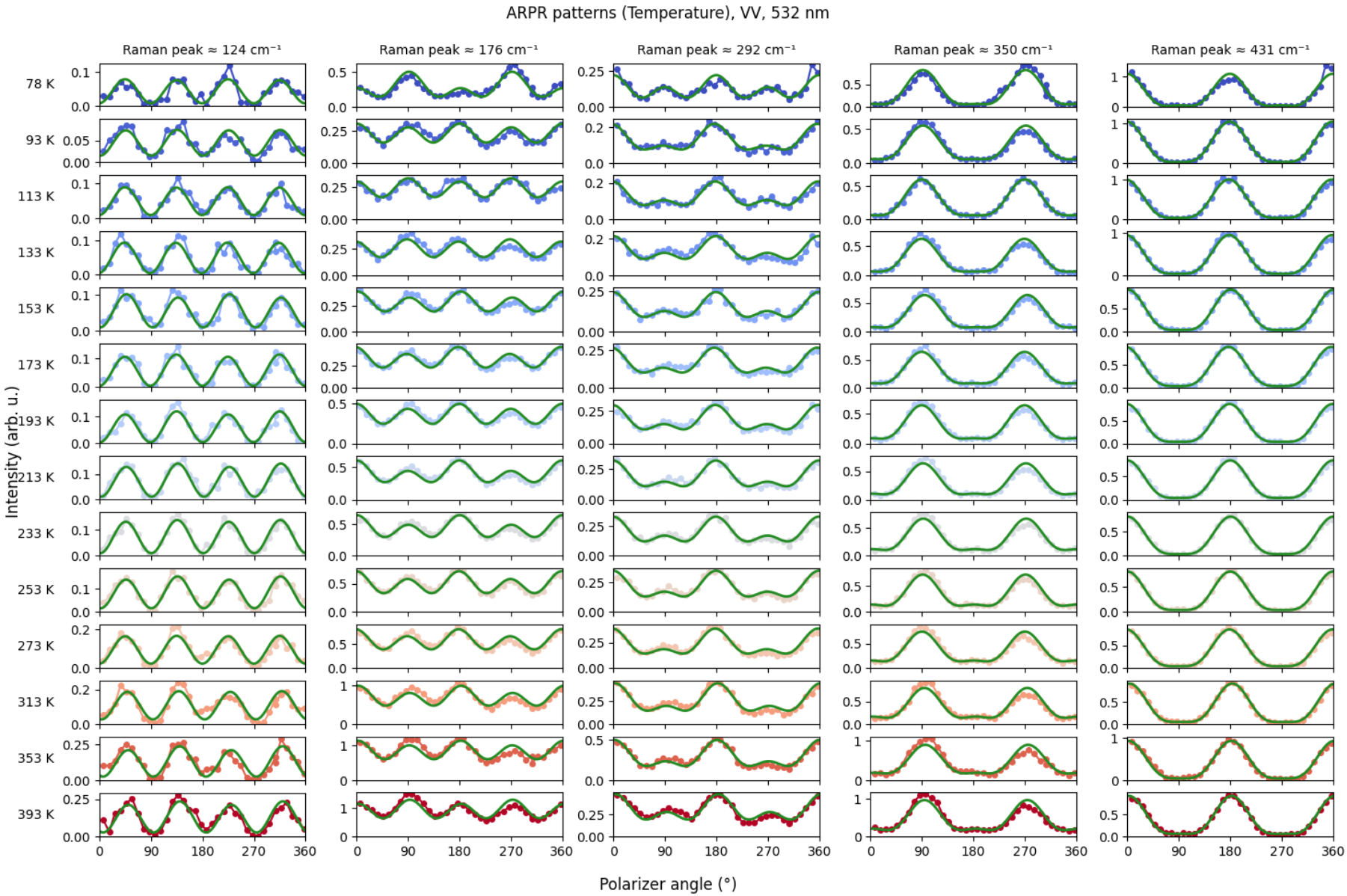

177 **Figure S11.** Temperature evolution of one-dimensional ARPR angular cuts of the intensity of $MoOCl_2$ Raman modes for 532 nm (VV regime). Dots
178 represent experimental data, and solid curves – fit using Eq. (2). The electric field is aligned with the *a* axis at polarization angles of 0° and 180°, and
179 with the *b* axis at 90° and 270°.

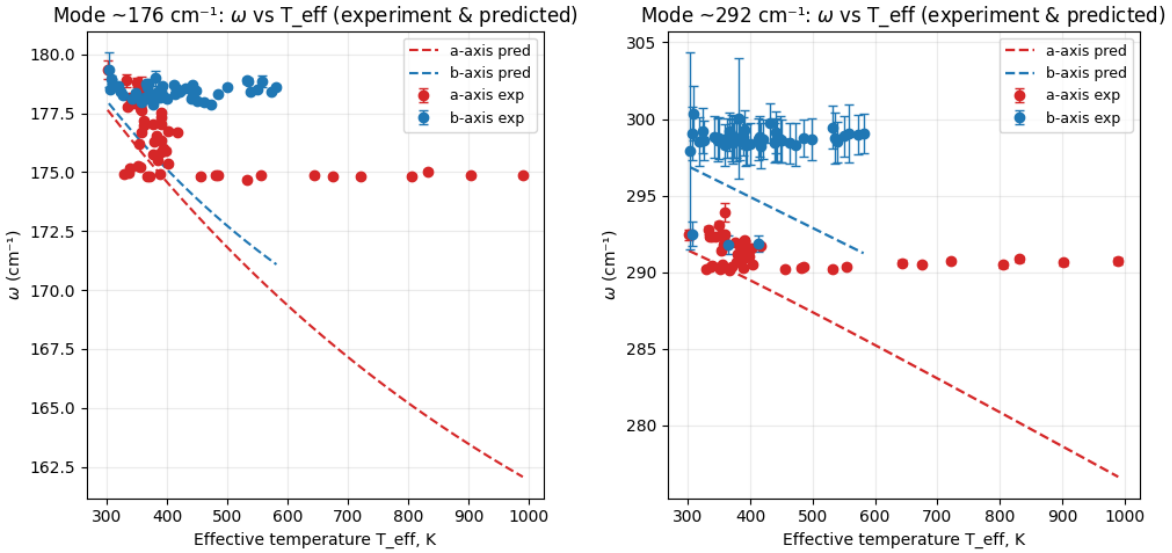

Figure S12. Frequency of the ~176 cm^{-1} (left) and ~292 cm^{-1} (right) modes as a function of effective temperature T_{eff}, highlighting the origin of the $\omega_{exp} - \omega_{pred}$ discrepancy in **Figure 3f**. Solid symbols show the experimentally extracted phonon frequency for excitation polarized along the *a* (red) and *b* (blue) axes as T_{eff} is increased using the Stokes/anti-Stokes thermometer of the same mode. Dashed lines are the corresponding frequencies predicted from the anharmonic thermal calibration, i.e., assuming that the mode follows its equilibrium softening $\omega(T)$ when the lattice is heated to T_{eff}. While the predicted frequency rapidly redshifts with increasing T_{eff}, the measured ω remains essentially constant, demonstrating directly that the vibrational population inferred from the Stokes/anti-Stokes ratio is strongly out of equilibrium with the phonon self-energy that governs the mode frequency.

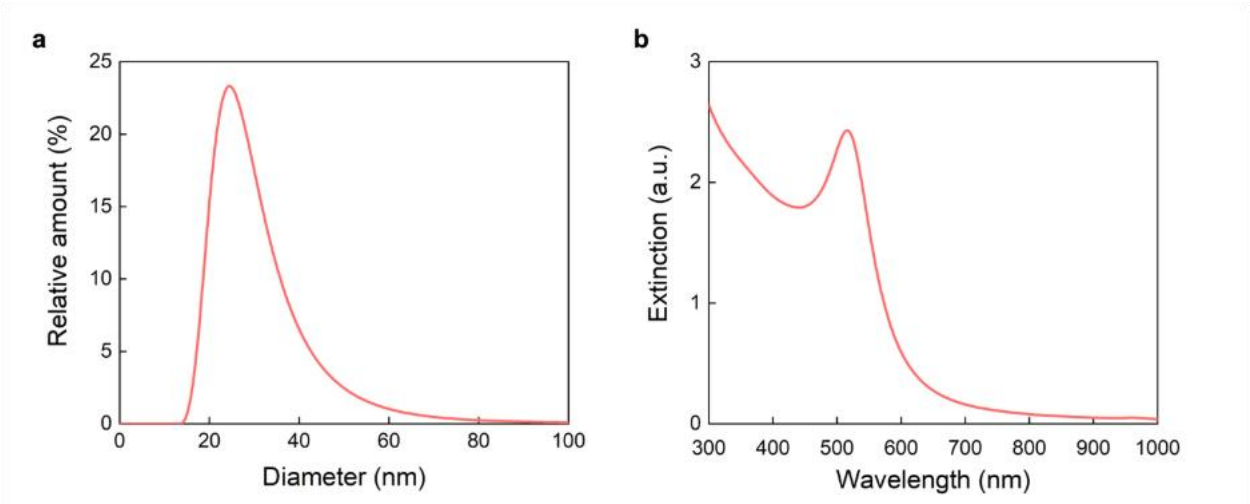

Figure S13. Characterization of laser-synthesized Au NPs: (a) hydrodynamic size distribution, (b) optical extinction spectra.

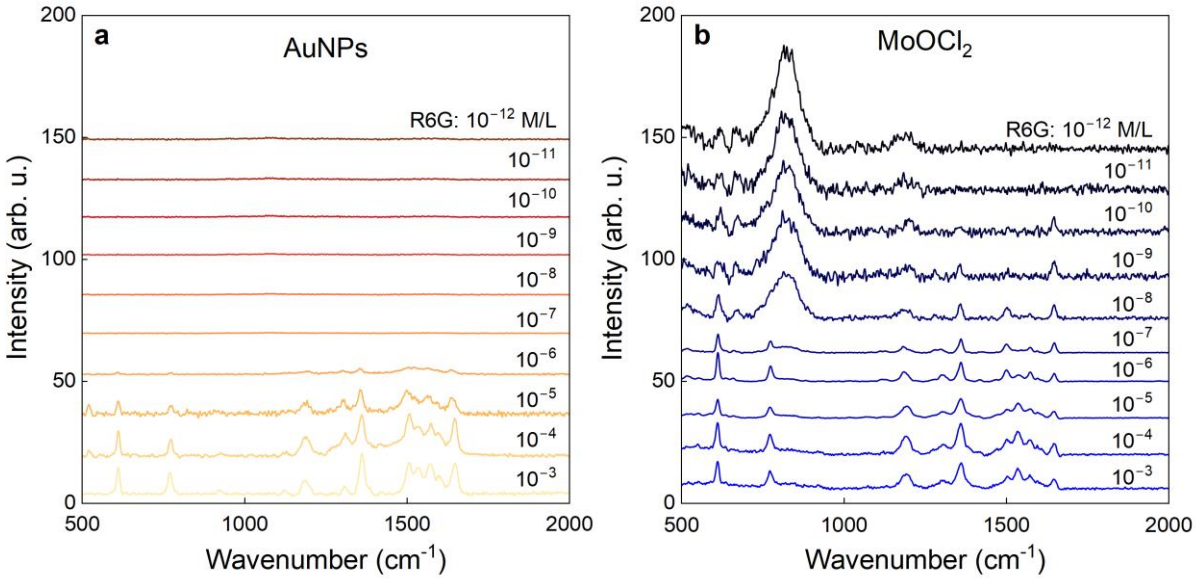

194

195 **Figure S14.** Representative normalized plots of R6G spectra on (a) Au nanoparticles (AuNPs) and
196 (b) $MoOCl_2$ flake (single spectra with polarizer aligned with *a*-axis).

197